

Uncertainty Bounds for Multivariate Machine Learning Predictions on High-Strain Brittle Fracture

Cristina Garcia-Cardona^{a,*}, M. Giselle Fernández-Godino^b, Daniel O'Malley^c and Tanmoy Bhattacharya^d

^aMS B256, Information Sciences Group (CCS-3), Los Alamos National Laboratory, Los Alamos, NM 87545

^bL-103, Atmospheric Science Research & Applications Group, AEED, Lawrence Livermore National Laboratory, 7000 East Ave, Livermore, CA 94550

^cMS D446, Computational Earth Sciences Group (EES-16), Los Alamos National Laboratory, Los Alamos, NM 87545

^dMS B285, Nuclear and Particle Physics, Astrophysics & Cosmology Group (T-2), Los Alamos National Laboratory, Los Alamos, NM 87545

ARTICLE INFO

Keywords:

machine learning
crack statistics
uncertainty quantification
heteroscedastic approach

ABSTRACT

Simulation of the crack network evolution on high strain rate impact experiments performed in brittle materials is very compute-intensive. The cost increases even more if multiple simulations are needed to account for the randomness in crack length, location, and orientation, which is inherently found in real-world materials. Constructing a machine learning emulator can make the process faster by orders of magnitude. There has been little work, however, on assessing the error associated with their predictions. Estimating these errors is imperative for meaningful overall uncertainty quantification. In this work, we extend the heteroscedastic uncertainty estimates to bound a multiple output machine learning emulator. We find that the response prediction is robust with a somewhat conservative estimate of uncertainty.

1. Introduction

Emulators based on machine learning (ML) have proven to be powerful tools for prediction. These techniques can decode complex coupling between variables, producing surrogates that require substantially reduced computational resources. Nevertheless, ML emulators, particularly those built using deep learning, have been strongly criticized because of their “black box” character, resulting in their cautious adoption in computational science. This criticism is ameliorated by uncertainty quantification (UQ) methods that can bound the calculation errors. Moreover, in numerous fields, such as medicine or engineering, it is essential to be able to estimate the level of confidence in the predictions of the model [1]. Uncertainty quantification encompasses a series of mathematical techniques that characterize the space of outcomes of a model while considering that not all the parameters are precisely specified. As such, sensitivity analysis, data assimilation, design of experiments, and risk assessment are important applications of UQ [40]. Different techniques have been developed to try to overcome the difficulty of assessing uncertainties for complex ML emulators, including dropout [13] and deep ensembles [22], and for applications such as PDEs [46], stochastic PDEs [47], multiscale methods [6] and computer vision [18]. In this work, we extend tools to characterize heteroscedastic uncertainty [18] to the analysis of ML emulators with multiple outputs.

ML emulators have been successfully used for applications such as classification [42], regression [14], bridging

scales [34, 7, 44], and dimensionality reduction [9] problems. In recent years, there has been substantial growth in ML application for material science [39], in particular for bridging scales in fracture mechanics. One of the major challenges in this context is the discrepancy in scales between microscale cracks and the macroscale associated with bulk materials [41]. Recent work has utilized ML algorithms to study brittle material under low-strain-rate tensile dynamic loading [25, 15, 32]. The evolution, growth, and interaction of cracks is key to modeling damage behavior in several brittle materials such as granite, concrete, metals, and ceramics [24, 31, 10, 16]. A recent novel alternative is to bridge continuum and mesoscales by developing and implementing a continuum-scale effective-moduli constitutive model that is informed by crack statistics generated from the mesoscale simulations in low-strain-rate [43] or high-strain-rate [23] conditions. However, the cost of generating large datasets can also be prohibitive if this comes from computationally intensive high-fidelity simulations. Previous work [12] showed that an inexpensive ML emulator can inform effective moduli when trained using damage and stress information from a mesoscale model. The ML emulator can then be combined with a continuum-scale hydrodynamic simulator to make accurate predictions inexpensively. In this work, we go a step forward and propose a technique to assign the ML emulator uncertainty bounds that can quantify its confidence taking into account the training data variability.

2. Problem of Interest

We study the damage behavior of beryllium under dynamic loading conditions. The experiment is based on a flyer disc impact against a target disc specimen (Cady et al. [3]). The beryllium samples were machined from a vacuum hot-

*Corresponding author

✉ cgarciac@lanl.gov (C. Garcia-Cardona); fernandez48@llnl.gov (M.G. Fernández-Godino); omalley@lanl.gov (D. O'Malley); tanmoy@lanl.gov (T. Bhattacharya)

ORCID(s): 0000-0002-5641-3491 (C. Garcia-Cardona); 0000-0002-3837-8661 (M.G. Fernández-Godino); 0000-0003-0432-3088 (D. O'Malley); 0000-0002-1060-652X (T. Bhattacharya)

Parameter	Value
Beryllium grade	S200F
Flyer disc height	2mm
Target disc height	4mm
Flyer/target disc diameter	28.8mm
Flyer/target flat within	2 μ m
Flyer/target parallel within	3 μ m
Density	1.85g/cm ³
Beryllium content	0.72wt.%
Average grain size	11.4 μ m
Polish	1 μ m diamond paste
Longitudinal wave sound speed	[13.19 – 13.20]mm/ μ s
Shear wave sound speed	[9.04 – 9.07]mm/ μ s

Table 1

Details for the Beryllium experimental samples.

pressed billet of beryllium S200F grade. Table 1 shows the main details of the beryllium disc composition, machining, and dimensions.

For validation purposes, the geometry, the size, the material properties, and the initial loading of the experiments were reproduced in simulations as closely as possible. The simulations were two-dimensional and modeled a beryllium flyer plate impact against a beryllium target specimen. Figure 1 is a schematic of the simulation setup. The flyer and target have a width of 28.8mm, the height of the target is 4mm, and the height of the flyer plate is 2mm. The flyer plate has an initial vertical velocity of 0.721 km/s towards the target plate, and the total simulation time is 1.2 μ s. A velocity tracer was placed at the middle rear of the target plate to measure the shock wave profiles for comparison with the experiments that we use to validate our approach.

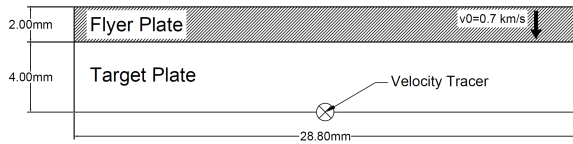


Figure 1: Initial setup for the flyer plate test simulations. The flyer plate has an initial velocity of 0.721km/s and it is initially in contact with the target plate.

After the impact, the target plate is subject to a strong compression that later becomes tension as the shock wave travels within the material and bounces against the borders of the plate. This indirect uniaxial tensile load leads to a Mode I crack growth dominated problem (the loading is applied perpendicular to the crack). The nature of fracture in flyer plate experiments leads to a non-homogeneous damage distribution where a concentrated region of damage forms across the target plate's midspan. In contrast, the majority of the plate remains relatively undamaged. For more information on flyer plate experiments, the reader can refer to the references [3, 4].

2.1. HOSS Model

In this work, we use the Hybrid Optimization Software Suite (HOSS) [35, 21, 20] high-fidelity model. We selected this finite-discrete-element method (FDEM) because it can model the evolution of the microcrack network in high-strain rate problems. HOSS was used to generate the training data needed to build the ML emulator described in Section 3. Modeling samples in HOSS is done by using discrete elements that are further divided into finite elements. The governing equations are conservation of mass, momentum, and energy along with Newton's laws [26, 28, 29, 30, 36, 27] and time-integration is done using a central difference scheme [37]. The cracks are located in the boundary of the finite elements, and often hundreds of elements are needed to model a single fracture [29]. The fine grids required, along with the explicit integration scheme, result in very expensive simulations.

HOSS has been validated against experiments in a number of settings including Split Hopkinson Bar tests on granite [36], failure processes in shale [5], earthquakes [19], and fracture coalescence processes in granite [11]. HOSS can also account for deformation in metals through a recent plasticity model [38]. HOSS explicitly accounts for crack nucleation, evolution, and coalescence. However, it does not account for microstructure, deformation twinning, dislocations, or atomic breaking at crack tips. The problem of interest in this work can be considered a pure tension problem dominated by opening failure. Still, since not every discrete element edge is oriented orthogonally to the applied load in HOSS, both shear and tearing modes occur at a local mesh element scale. The connections between finite elements are made using springs, so if two elements are pulled apart, a small space appears between them. This also allows one element to slide relative to another.

A single simulation of the flyer plate problem, whose detailed description can be found in Section 2, requires 87,066 elements in HOSS to describe the crack dynamics accurately. The simulations use 160 processor hours and produce 23 GBs of simulation data. HOSS is a deterministic model; hence, to obtain the statistical variability naturally existent in materials, we randomly generate the initial crack location, orientation, and length—running a total of 100 HOSS simulations. The HOSS computational cost associated is prohibitive for many applications where multiple simulations are needed, such as optimization and UQ, leading to the need for cheaper ML emulators.

Each simulation spans 1.2 μ s using HOSS time steps of $10^{-5}\mu$ s, with outputs every 0.0025 μ s, which we refer to as a time step—each simulation is thus 480 time-steps long. There are 200 initial cracks, and they are only imposed in the target specimen. A uniform distribution is used to determine the initial crack location (x, y) within the target plate. The horizontal coordinate distribution is $x \sim U[0, 28.8\text{mm}]$ while the vertical coordinate distribution is $y \sim U[0, 4\text{mm}]$ (see Figure 1). The initial orientation of the cracks (θ) follows the uniform distribution $\theta \sim U[0^\circ, 180^\circ]$. The initial crack lengths are determined based on a power-law proba-

bility density function [2, 17], and the lengths vary between 0.1mm and 0.3mm . The location, length, and orientation distributions generate only the initial conditions for the crack network within the target plate and are changed randomly in every simulation. The evolution of the crack network takes place within the HOSS simulations. The probability density function (power-law function) used to generate the initial crack length distribution on the target plate, $f_1(a, t = 0)$, is

$$f_1(a, t = 0) = \frac{qa^{(q-1)}}{a_2^q - a_1^q}, \quad (1)$$

where $q = -3$, $a_1 = 0.1$, $a_2 = 0.3$, and a is a real number in the range $[a_1, a_2]$. The end values a_1 and a_2 are the initial minimum and maximum crack length. Therefore,

$$f_1(a, t = 0) \approx \frac{a^{-4}}{321}. \quad (2)$$

The time-dependent crack probability density function is obtained from each HOSS simulation after its completion. Figure 2 shows the shock wave velocity at the initial, intermediate and final time ($t = 0$, $t = 0.6\mu\text{s}$, $t = 1.2\mu\text{s}$, respectively) for a HOSS simulation of the flyer plate problem. At $t = 1.2\mu\text{s}$, it is observed that the failure is produced in the middle section of the target plate because the target plate is twice the height of the flyer plate (see Figure 1). Note that nucleation and coalescence of cracks occur as the simulation proceeds.

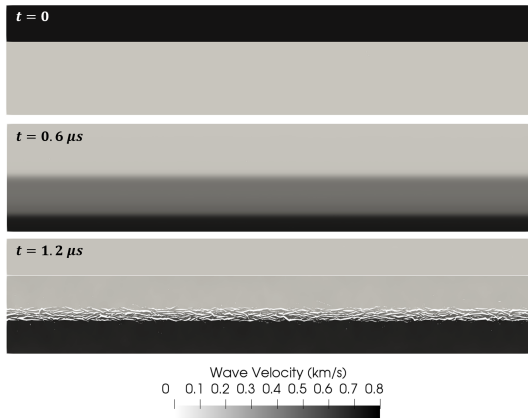


Figure 2: HOSS simulation. Shock wave velocity at initial, intermediate and final times.

3. Uncertainty Quantification of Machine Learning Emulator

The goal of UQ is to assign a level of confidence to ML emulator predictions. In turn, this assignment can be used to estimate decision risks or provide a principled selection mechanism of the most impactful experiments: the ones that minimize the uncertainty. In the case of ML emulators, the UQ approaches are designed to predict both the regular input-output mapping between features and quantities of interest,

together with an additional set of outputs intended to capture the level of confidence in the ML emulator predictions. Here we use a heteroscedastic [18] set up to represent the uncertainty in the regressor emulator. The heteroscedastic formulation characterizes the output of the regression emulator as a normally-distributed random variable with parameters that are feature-dependent, i.e., the variance of the predictions is heterogeneous and domain-dependent. In contrast with many applications that consist of only one output, we explore the case of UQ for emulators with multiple outputs. Further, we develop a framework for constructing multivariate heteroscedastic UQ bounds.

3.1. Machine Learning Emulator

Since simulating the evolution of the microcrack network in high-strain rate problems is computationally very expensive, ML emulators are gaining traction as alternative data-driven surrogate emulators for this application. With enough data, these emulators can synthesize the system's dynamics, achieving accuracy comparable to the high-fidelity models. At the same time, they are more computationally efficient and require much less time for evaluation.

In previous work [12], we demonstrated that a recurrent neural network (RNN) was able to predict two quantities of interest, namely the length of the longest crack, L_{long} , and the maximum tensile stress, S_{yy} , as a function of time for the flyer plate problem described in Section 2. In this work, we go a step forward, and we estimate the uncertainty in the one-time-step response prediction of the coupled system formed by the same quantities of interest: L_{long} and S_{yy} . The more complex task of estimating uncertainties in a multivariate RNN emulator will be addressed in future work.

To build the emulator, the quantities of interest are paired at each time step t as

$$\left(L_{\text{long}}^{(t)}, S_{yy}^{(t)} \right). \quad (3)$$

Given a sequence of d consecutive time steps:

$$\left[\left(L_{\text{long}}^{(t-d)}, S_{yy}^{(t-d)} \right), \dots, \left(L_{\text{long}}^{(t-2)}, S_{yy}^{(t-2)} \right), \left(L_{\text{long}}^{(t-1)}, S_{yy}^{(t-1)} \right) \right], \quad (4)$$

the emulator is trained to predict the next pair in the time sequence $\left(L_{\text{long}}^{(t)}, S_{yy}^{(t)} \right)$. Accordingly, the input patterns for the emulator conform to sequences as the one in (4), while the output consist of pairs as in (3). To simplify the notation the i -th input pattern is denoted by \mathbf{x}_i and the corresponding output pair is denoted by \mathbf{y}_i . Hence, the training data set is denoted as the collection $\{\mathbf{x}_i, \mathbf{y}_i\}_{i=1}^N$, where $\mathbf{x}_i \in \mathbb{R}^{2d}$, $\mathbf{y}_i \in \mathbb{R}^2$ and N represents the number of samples in the training set.

We design the emulator as a multilayer feed-forward neural network composed of neurons with dense connections. The output o_j^i of each artificial neuron j in layer i is computed as

$$o_j^i = h \left(\mathbf{w}_j^i \cdot \boldsymbol{\xi}^i + b_j^i \right), \quad (5)$$

where ξ^i represents the input vector at layer i ; \mathbf{w}_j^i and b_j^i represent neuron parameters: weight vector and bias, respectively; the operator \cdot denotes a dot product; and h , the activation function. The activation function used is a rectified linear unit (ReLU) and corresponds to the following operation: $\text{ReLU}(v) = \max(0, v)$.

In a feed-forward network, the information propagates layer-wise: the input vector ξ^i at layer i is constructed by concatenation of the outputs of the neurons at layer $i - 1$, with layer 0 being the input layer and the last layer being the output layer, whose output constitutes the output of the network. Intermediate layers (i.e., different from the input and output layers) are called hidden layers. The overall mapping computed by the neural network can be denoted as $f(\mathbf{x})$ (or $\mathbf{f}(\mathbf{x})$ for an emulator with multiple outputs). In a supervised setup, the performance of the network is quantified by a loss function that measures the difference between the expected outputs, corresponding to the outputs of the training set $\{\mathbf{y}_i\}$, and the outputs computed by the emulator $\{\mathbf{f}(\mathbf{x}_i)\}$. Training the emulator implies minimizing the loss function with respect to the emulator parameters, i.e., the weights and biases of all the neurons in the network. Because we are also interested in predicting the uncertainty, the approach is modified to include additional outputs for the uncertainty estimation and to optimize a loss function that considers the uncertainty explicitly. Section 3.2 describes this modification in detail.

3.2. Heteroscedastic Approach

A heteroscedastic uncertainty estimate assigns a different uncertainty to each sample. Specifically, the heteroscedastic formulation assumes that the prediction can be modeled as a normal random variable with domain-dependent parameters. Often the heteroscedastic formulation is applied to regression emulators of only one output. Thus, the ML emulator learns two outputs: the regular regression prediction $f(\mathbf{x}_i)$, which corresponds to the mean, and the uncertainty represented by an additional output $\sigma(\mathbf{x}_i)^2$, which corresponds to the variance of the normal distribution.

The emulator is trained by minimizing the heteroscedastic loss over the entire dataset,

$$\mathcal{L}(y, f, \sigma) = \frac{1}{N} \sum_{i=1}^N \frac{1}{2\sigma(\mathbf{x}_i)^2} \|y_i - f(\mathbf{x}_i)\|^2 + \frac{1}{2} \log \sigma(\mathbf{x}_i)^2. \quad (6)$$

This loss function, patterned after the likelihood of a normal distribution, is composed of two terms: a first term that is a weighted mean squared error (MSE), where large error predictions are compensated by large variances, and a second term that penalizes those large variances. Note that the loss function uses the fact that the expected output y_i for input \mathbf{x}_i is known, but the uncertainty is not. In other words, the training of the regular output is supervised since the ground-truth is given. In contrast, the training of the uncertainty is unsupervised since the true σ_i is not available. The balance between the first and second loss terms allows determining an ‘optimal’ uncertainty prediction. Hence, while the out-

put prediction can exploit the available data directly, the uncertainty prediction is a much harder task, and underlying assumptions, like model smoothness, play a greater role in determining the kind of functions that can be induced as uncertainty estimators under this formulation.

3.2.1. Multivariate Approach

When the prediction includes multiple outputs, a one-dimensional normal random variable approach is not enough to capture the influence of each in the uncertainty prediction of the others. In that case it is necessary to adapt the formulation of the heteroscedastic loss to consider the probability density function (PDF) of a multivariate normal distribution. The multivariate normal distribution PDF can be written as

$$\mathcal{N}(\boldsymbol{\mu}, \Sigma) = \frac{\det(\Sigma)^{-1/2}}{2\pi^{k/2}} \exp\left(-\frac{1}{2}(\mathbf{z} - \boldsymbol{\mu})^T \Sigma^{-1}(\mathbf{z} - \boldsymbol{\mu})\right), \quad (7)$$

where $\boldsymbol{\mu} \in \mathbb{R}^k$ stands for the mean, $\Sigma \in \mathbb{R}^{k \times k}$ represents the positive covariance matrix, and k is the space dimension. The multivariate heteroscedastic loss is expressed then as the negative log-likelihood (NLL) of the multivariate PDF with parameters promoted to functions of the input,

$$\begin{aligned} \mathcal{L}(\mathbf{y}, \mathbf{f}, \Sigma) = & \\ & \frac{1}{N} \sum_{i=1}^N \left((\mathbf{y}_i - \mathbf{f}(\mathbf{x}_i))^T \Sigma(\mathbf{x}_i)^{-1} (\mathbf{y}_i - \mathbf{f}(\mathbf{x}_i)) \right. \\ & \left. + \log \det(\Sigma(\mathbf{x}_i)) \right), \end{aligned} \quad (8)$$

where constants $(2\pi)^{-k/2}$ and $1/2$, have been omitted because they do not change the optimum.

Correspondingly, this approach has to be designed to predict a vector $\mathbf{f}(\mathbf{x}_i) \in \mathbb{R}^k$, with the k outputs of the regular emulator and a matrix $\Sigma(\mathbf{x}_i) \in \mathbb{R}^{k \times k}$ representing the covariance matrix for the UQ estimation.

The critical component of the multivariate heteroscedastic approach is being able to guarantee that the covariance matrix, Σ , is positive definite. An efficient strategy to achieve this is to formulate the learning task such that a matrix $A^T A$, which is positive by definition, is learned instead. This is a general strategy that can be applied to produce uncertainty estimates for ML emulators with two or more outputs.

3.2.2. The Two-Outputs Case

In this section, we show the specific structure of the task for a two-output emulator, since this is the case of interest for this work.

The heteroscedastic UQ for an emulator with two outputs has the following structure:

- Base outputs: two to predict the mapping $\mathbf{f}(\mathbf{x}_i) \in \mathbb{R}^2$,
- Additional outputs: four to predict the components of matrix $A(\mathbf{x}_i) \in \mathbb{R}^{2 \times 2}$. For simplicity, the explicit \mathbf{x}_i dependence of A is (mostly) omitted in the following description.

The 2×2 matrix A can be represented in terms of scalar components a, b, c, d , as

$$A = \begin{pmatrix} a & b \\ c & d \end{pmatrix},$$

which in turn yields the covariance matrix

$$\begin{aligned} \Sigma &= A^T A = \begin{pmatrix} a & b \\ c & d \end{pmatrix}^T \begin{pmatrix} a & b \\ c & d \end{pmatrix} \\ &= \begin{pmatrix} a^2 + c^2 & ab + cd \\ ab + cd & b^2 + d^2 \end{pmatrix} \triangleq \begin{pmatrix} \sigma_{11}^2 & \sigma_{12} \\ \sigma_{12} & \sigma_{22}^2 \end{pmatrix}. \end{aligned} \quad (9)$$

Since any simultaneous rotation of the vectors given by the columns of matrix A by the same angle leaves the covariance matrix unchanged, we choose rotation angle $\theta = \arctan(c - b)/(a + d)$, to force $b = c$. Thus, the UQ approach is built to have only five outputs: two for $\mathbf{f}(\mathbf{x}_i)$ and three for the distinct components of matrix $\Sigma(\mathbf{x}_i)$: $\sigma_{11}(\mathbf{x}_i)$, $\sigma_{12}(\mathbf{x}_i)$, $\sigma_{22}(\mathbf{x}_i)$.

Further simplifications can be achieved by applying the following observations. For a positive definite covariance matrix $\Sigma \in \mathbb{R}^{2 \times 2}$, the inverse can be computed analytically as

$$\Sigma^{-1} = \frac{1}{\det(\Sigma)} \begin{pmatrix} \sigma_{22}^2 & -\sigma_{12} \\ -\sigma_{12} & \sigma_{11}^2 \end{pmatrix}, \quad (10)$$

with $\det(\Sigma) = \sigma_{11}^2 \sigma_{22}^2 - \sigma_{12}^2 \neq 0$. Defining: $\mathbf{e} = (e_1, e_2)^T = \mathbf{y} - \mathbf{f}(\mathbf{x})$, i.e., the difference between the ground truth \mathbf{y} and the mean prediction $\mathbf{f}(\mathbf{x})$, allows to write

$$\begin{aligned} \text{NLL} &= \frac{1}{\det(\Sigma)} \begin{pmatrix} e_1 \\ e_2 \end{pmatrix}^T \begin{pmatrix} \sigma_{22}^2 - \sigma_{12} \\ -\sigma_{12} \sigma_{11}^2 \end{pmatrix} \begin{pmatrix} e_1 \\ e_2 \end{pmatrix} + \log \det(\Sigma) \\ &= \frac{1}{\det(\Sigma)} (\sigma_{22}^2 e_1^2 - 2 \sigma_{12} e_1 e_2 + \sigma_{11}^2 e_2^2) + \log \det(\Sigma). \end{aligned} \quad (11)$$

Hence, the loss function for a heteroscedastic approach with two outputs corresponds to

$$\begin{aligned} \mathcal{L}(\mathbf{y}, \mathbf{f}, \Sigma) &= \frac{1}{N} \sum_{i=1}^N \left(\frac{1}{\det(\Sigma(\mathbf{x}_i))} (\sigma_{22}(\mathbf{x}_i)^2 (y_1 - f_1(\mathbf{x}_i))^2 \right. \\ &\quad \left. - 2 \sigma_{12}(\mathbf{x}_i) (y_1 - f_1(\mathbf{x}_i)) (y_2 - f_2(\mathbf{x}_i)) \right. \\ &\quad \left. + \sigma_{11}(\mathbf{x}_i)^2 (y_2 - f_2(\mathbf{x}_i))^2) + \log \det(\Sigma(\mathbf{x}_i)) \right). \end{aligned} \quad (12)$$

In summary, for a two-output heteroscedastic UQ estimate, a neural network with $2d$ inputs and five outputs is built, and its parameters are determined by the minimization of the loss function (12).

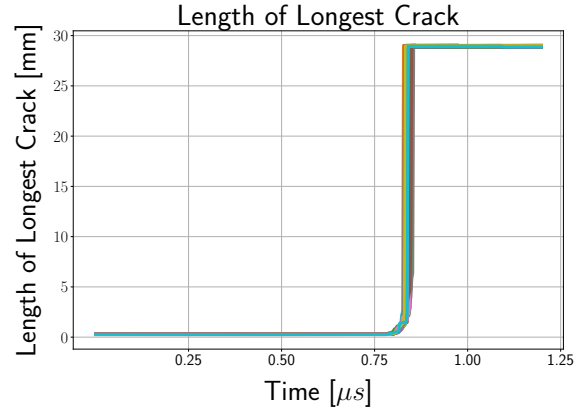
4. Results

As mentioned before, the focus of this work is estimating the uncertainty in the one-time-step response prediction of

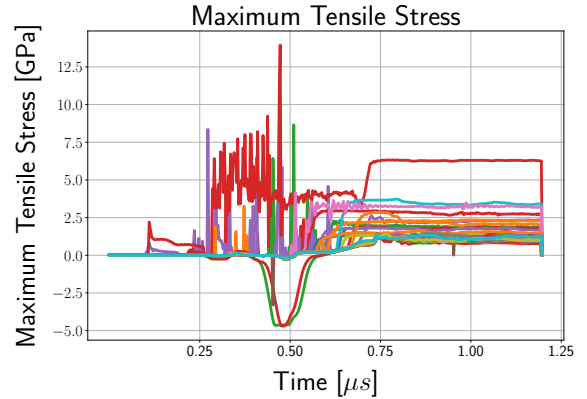
two quantities of interest: length of the longest crack (L_{long}) and the maximum tensile stress (S_{yy}) for the flyer plate problem described in Section 2. For this purpose, a feed-forward neural network was constructed, and its performance was compared against different experimental setups.

4.1. Simulation Data

Similarly to [12], 100 HOSS flyer plate simulations described in Sec. 2.1 were used. Each simulation includes time series of 480 time steps for different quantities of interest. From each of the 100 simulations the output of interest, L_{long} and S_{yy} , are extracted. Figure 3(a) and Figure 3(b) show L_{long} and S_{yy} , respectively as a function of time.



(a) Evolution of length of the longest crack L_{long} .



(b) Evolution of maximum tensile stress S_{yy} .

Figure 3: The 100 different HOSS simulations used for train and test the ML emulator.

Since the task is one-time-step prediction, each time series is split into subsequences containing $d + 1$ time steps each, where the first d constitutes the input pattern \mathbf{x} and the last the output \mathbf{y} . Remember that because we are interested in the L_{long} and S_{yy} interaction, the input subsequences are paired as in Eq. (4), while the output consists of pairs as in Eq. (3), with dimensionalities $\mathbf{x} \in \mathbb{R}^{2d}$ and $\mathbf{y} \in \mathbb{R}^2$, respectively. To guarantee that subsequences of the same simulation are not mixed during training and testing, they are first split randomly into 80% simulations for training and 20% simulations for testing. Afterward, they are further split

Embedding Dimension	Subsequences	Training Set	Testing Set
$d = 10$	469	37,520	9,380
$d = 20$	459	36,720	9,180
$d = 30$	449	35,920	8,980

Table 2

Data sets for one-time-step prediction.

into subsequences to build the corresponding sets, keeping subsequences of the training simulations in the training set and subsequences of the testing simulations in the testing set. Different embedding dimensions d are used. The sizes of the resulting sets are summarized in Table 2. Note that d input components are needed to predict the $d + 1$ component, meaning that some of the left-most values in the simulation do not have enough previous elements to build the input pattern. Consequently, the resulting number of usable subsequences slightly decreases when d increases.

4.2. Model Performance

A feed-forward neural network with two hidden layers of 200 neurons each and output layer of five neurons was constructed. A different emulator was trained for each of the different embedding dimensions. The corresponding networks have (45,405), (49,405), and (53,405) parameters, respectively. Each emulator is trained for 50 epochs with batch size of five. The training process is repeated 20 times, using different training-testing partitions. The neural network emulators were built and trained with the Python package Keras [8]. To quantify the emulator performance, the coefficient of determination (R^2),

$$R^2(y, \hat{y}) = 1 - \frac{\sum_{i=1}^n (y_i - \hat{y}_i)^2}{\sum_{i=1}^n (y_i - \bar{y})^2}, \quad \bar{y} = \frac{1}{n} \sum_{i=1}^n y_i, \quad (13)$$

was used, as computed by the Scikit-learn Python package [33] and reported in Table 3 as the average and standard deviation over the 20 repetitions evaluated in the testing set (i.e. the set held out during training). As the table shows, the performance in terms of R^2 is good, specially for L_{long} , and the predictions with embedding dimension $d = 20$ is slightly better than the other two cases.

Note, however, that the R^2 score only takes into account the predicted values $\mathbf{f}(\mathbf{x})$, so another metric is required to evaluate the predicted uncertainty. For this purpose, we estimate the emulator coverage, which evaluates how many times the prediction falls inside the confidence interval corresponding to a specified ventile [45]. The closer the fraction of points inside the interval and the ventile are, the tighter the predicted uncertainties.

Estimating the Emulator Coverage

To estimate the emulator coverage, it is necessary to calculate the expected fraction inside specified contour levels of the multivariate normal distribution. Contours of the multivariate normal distribution are the set of values where the argument of the exponential in the PDF is the same. As described in Appendix A, for data in \mathbb{R}^2 , each contour corre-

Embedding Dimension	R^2	
	L_{long}	S_{yy}
$d = 10$	0.97 ± 0.03	0.87 ± 0.22
$d = 20$	0.97 ± 0.02	0.89 ± 0.09
$d = 30$	0.95 ± 0.05	0.86 ± 0.10

Table 3
 R^2 : Mean \pm standard deviation.

sponds to an ellipse, which can be expressed as $\gamma = -2 \ln \alpha$, with α corresponding to the coverage (i.e. $1 - \alpha$ equates to the confidence level) and $\gamma = (\mathbf{z} - \boldsymbol{\mu})^T \boldsymbol{\Sigma}^{-1} (\mathbf{z} - \boldsymbol{\mu})$, the level of the contour.

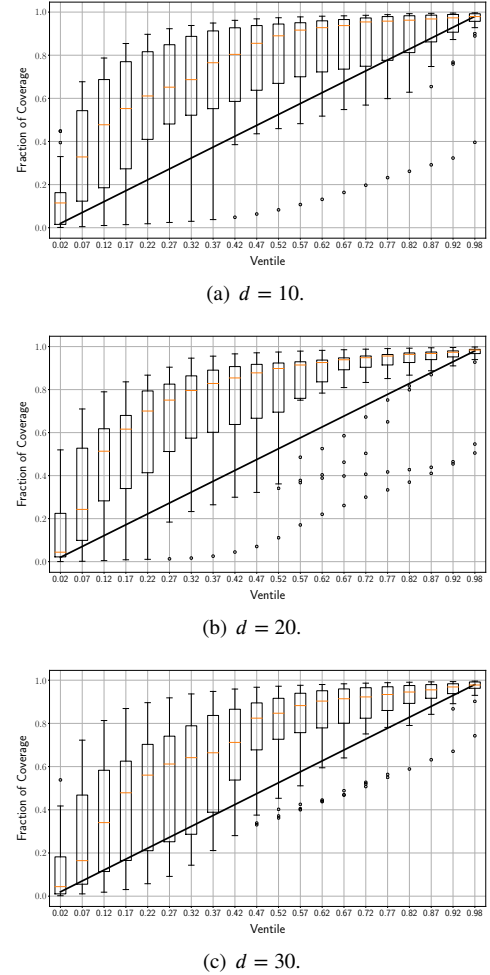

Figure 4: Box plots of fraction of coverage for $d = 10, 20, 30$ over 20 repetitions of the heteroscedastic approach.

Figure 4 displays the evaluation of the emulator coverage. This is represented by box plots computed from the coverage fractions associated with the predictions made by the emulator, for the testing sets over the 20 repetitions, as a function of the specified ventile. The box plot's meaning is as follows: the box is plotted between the first and third quartiles, the orange line inside the box is the median, the difference between the third and the first quartile is the interquartile range (IQR). The whiskers extend between a distance of 1.5 times the IQR below the lower quartile and a distance of

1.5 times the IQR above the upper quartile. Other observed points outside the whiskers are plotted as outliers. Additionally, the ideal relationship between coverage and ventile is plotted as a continuous black line. It can be seen that all the emulators tend to overestimate the confidence interval, which implies that the uncertainty estimation is conservative, i.e., biased towards the safer side of including more fraction of predictions than what could be inferred from the ventile. Also, the medians observed tend to be closer to the ideal for $d = 10$ and $d = 30$ than for $d = 20$, with the best overall statistics for $d = 30$. This illustrates the tension between prediction and uncertainty estimation: the ranking of emulators by R^2 may differ from the one obtained by coverage.

5. Conclusion

Quantifying the uncertainty sources associated with physical models is of high importance for their credibility. When a machine learning emulator is used to speed up the process of predicting crack evolution in high-strain brittle experiments, it is important to evaluate the uncertainty associated with how well the machine learning emulator captures the underlying simulation. To some extent, this mitigates the undesirable “black box” nature of machine learning emulators. It does not make the predictions interpretable, but instead gives an indication of the expected accuracy of the prediction.

The main contribution of this work is to use machine-learning itself to bound the multivariate response of such an emulator using a heteroscedastic approach. The machine learning response prediction is robust, while uncertainty predictions conservatively overestimate the coverage for the given confidence levels. Thus, for example, the 95% confidence interval covers about 97.6% of the data. This behavior is much more desirable than underpredicting the uncertainty. Underpredicting the uncertainty would make the predictions seem more accurate than they are, which could have serious undesirable consequences in contexts where safety relies on the material response. The underlying cause of this overprediction is probably a non-normal distribution of the uncertainty, especially near a failure point, and points to the need for a nonparametric estimator for the uncertainty. We leave that development to future work.

CRedit authorship contribution statement

Cristina Garcia-Cardona: Conceptualization, Methodology, Software, Formal analysis, Visualization, Writing - Original Draft, Writing - Review & Editing. **M. Giselle Fernández-Godino:** Conceptualization, Investigation, Software, Formal analysis, Visualization, Writing - Original Draft, Writing - Review & Editing. **Daniel O'Malley:** Conceptualization, Writing - Review & Editing. **Tanmoy Bhattacharya:** Conceptualization, Methodology, Supervision, Project administration, Writing - Review & Editing.

Data Availability

Available from the authors upon request.

Acknowledgements

MGFG and DO acknowledge support from the National Nuclear Security Administration's Advanced Simulation and Computing program. This work has been supported in part by the Joint Design of Advanced Computing Solutions for Cancer (JDACS4C) program established by the U.S. Department of Energy (DOE) and the National Cancer Institute (NCI) of the National Institutes of Health, and was performed under the auspices of the U.S. Department of Energy by Lawrence Livermore National Laboratory under Contract DE-AC52-07NA27344 and Los Alamos National Laboratory under Contract DE-AC5206NA25396. Approved for public release LA-UR-20-30015 and LLNL-JRNL-817876.

References

- [1] Begoli, E., Bhattacharya, T., Kusnezov, D., 2019. The need for uncertainty quantification in machine-assisted medical decision making. *Nature Machine Intelligence* 1, 20–23. doi:[10.1038/s42256-018-0004-1](https://doi.org/10.1038/s42256-018-0004-1).
- [2] Bonnet, E., Bour, O., Odling, N.E., Davy, P., Main, I., Cowie, P., Berkowitz, B., 2001. Scaling of fracture systems in geological media. *Reviews of geophysics* 39, 347–383. doi:[10.1029/1999RG000074](https://doi.org/10.1029/1999RG000074).
- [3] Cady, C.L., Adams, C.D., Prime, M.B., Hull, L.M., Addessio, F.L., Bronkhorst, C.A., Brown, E.N., Liu, C., Sisneros, T.A., Brown, D.W., et al., 2011. Characterization of S200-F Beryllium using shock loading and quasi-static experiments. Technical Report. LA-UR-11-06976, Los Alamos National Laboratory.
- [4] Cady, C. M. , Adams, C. D. , Hull, L. M. , Gray, G. T. , Prime, M. B. , Addessio, F. L. , Wynn, T. A. , Papin, P. A. , Brown, E. N. , 2012. Characterization of shocked beryllium. EPJ Web of Conferences 26, 01009. doi:[10.1051/epjconf/20122601009](https://doi.org/10.1051/epjconf/20122601009).
- [5] Carey, J.W., Lei, Z., Rougier, E., Mori, H., Viswanathan, H., 2015. Fracture-permeability behavior of shale. *Journal of unconventional oil and gas resources* 11, 27–43. doi:[10.1016/j.juogr.2015.04.003](https://doi.org/10.1016/j.juogr.2015.04.003).
- [6] Chan, S., Elsheikh, A.H., 2018. A machine learning approach for efficient uncertainty quantification using multiscale methods. *Journal of Computational Physics* 354, 493–511. doi:[10.1016/j.jcp.2017.10.034](https://doi.org/10.1016/j.jcp.2017.10.034).
- [7] Cheng, Y., Geng, J., Wang, Y., Li, J., Li, D., Wu, J., 2019. Bridging machine learning and computer network research: a survey. *CCF Transactions on Networking* 1, 1–15. doi:[10.1007/s42045-018-0009-7](https://doi.org/10.1007/s42045-018-0009-7).
- [8] Chollet, F., 2015. Keras documentation. URL: <https://keras.io/>.
- [9] Cichocki, A., Lee, N., Oseledets, I., Phan, A.H., Zhao, Q., Mandic, D.P., 2016. Tensor networks for dimensionality reduction and large-scale optimization: Part I low-rank tensor decompositions. *Foundations and Trends® in Machine Learning* 9, 249–429. doi:[10.1561/22000000059](https://doi.org/10.1561/22000000059).
- [10] Escobedo, J.P., Trujillo, C.P., Cerreta, E.K., Gray, G.T., Brown, E.N., 2014. Effect of shock wave duration on dynamic failure of tungsten heavy alloy. *Journal of Physics: Conference Series* 500, 112012. doi:[10.1088/1742-6596/500/11/112012](https://doi.org/10.1088/1742-6596/500/11/112012).
- [11] Euser, B., Rougier, E., Lei, Z., Knight, E.E., Frash, L.P., Carey, J.W., Viswanathan, H., Munjiza, A., 2019. Simulation of fracture coalescence in granite via the combined finite-discrete element method. *Rock Mechanics and Rock Engineering* 52, 3213–3227. doi:[10.1007/s00603-019-01773-0](https://doi.org/10.1007/s00603-019-01773-0).
- [12] Fernández-Godino, M.G., Panda, N., Larkin, K.C., Hunter, A., O'Malley, D., Haftka, R., Srinivasan, G., 2021. Accelerating high-strain continuum-scale brittle fracture simulations with machine

- learning. *Computational Materials Science* 186, 109959. doi:[10.1016/j.commatsci.2020.109959](https://doi.org/10.1016/j.commatsci.2020.109959).
- [13] Gal, Y., Ghahramani, Z., 2016. Dropout as a bayesian approximation: Representing model uncertainty in deep learning, in: Balcan, M.F., Weinberger, K.Q. (Eds.), *Proceedings of Machine Learning Research*, PMLR, New York, New York, USA. pp. 1050–1059. URL: <http://proceedings.mlr.press/v48/gal16.html>.
- [14] Huang, J.C., Ko, K.M., Shu, M.H., Hsu, B.M., 2020. Application and comparison of several machine learning algorithms and their integration models in regression problems. *Neural Computing and Applications* 32, 1–9. doi:[10.1007/s00521-019-04644-5](https://doi.org/10.1007/s00521-019-04644-5).
- [15] Hunter, A., Moore, B.A., Mudunuru, M., Chau, V., Tchoua, R., Nyshadham, C., Karra, S., O'Malley, D., Rougier, E., Viswanathan, H., Srinivasan, G., 2019. Reduced-order modeling through machine learning and graph-theoretic approaches for brittle fracture applications. *Computational Materials Science* 157, 87–98. doi:[10.1016/j.commatsci.2018.10.036](https://doi.org/10.1016/j.commatsci.2018.10.036).
- [16] Huq, F., Liu, J., Tonge, A., Graham-Brady, L., 2019. A micromechanics based model to predict micro-crack coalescence in brittle materials under dynamic compression. *Engineering Fracture Mechanics* 217, 106515. doi:[10.1016/j.engfracmech.2019.106515](https://doi.org/10.1016/j.engfracmech.2019.106515).
- [17] Ignatovich, S.R., Bourau, N.I., 2019. Power law of crack length distribution in the multiple damage process. *Strength of Materials* 51, 735–745. doi:[10.1007/s11223-019-00122-4](https://doi.org/10.1007/s11223-019-00122-4).
- [18] Kendall, A., Gal, Y., 2017. What uncertainties do we need in bayesian deep learning for computer vision?, in: Guyon, I., Luxburg, U.V., Bengio, S., Wallach, H., Fergus, R., Vishwanathan, S., Garnett, R. (Eds.), *Advances in Neural Information Processing Systems*, Curran Associates, Inc., pp. 5574–5584. URL: <https://proceedings.neurips.cc/paper/2017/file/2650d6089a6d640c5e85b2b88265dc2b-Paper.pdf>.
- [19] Klinger, Y., Okubo, K., Vallage, A., Champenois, J., Delorme, A., Rougier, E., Lei, Z., Knight, E.E., Munjiza, A., Satriano, C., et al., 2018. Earthquake damage patterns resolve complex rupture processes. *Geophysical Research Letters* 45, 10–279. doi:[10.1029/2018GL078842](https://doi.org/10.1029/2018GL078842).
- [20] Knight, E.E., Rougier, E., Lei, Z., 2015. Hybrid optimization software suite (HOSS)-educational version. Technical Report. LA-UR-15-27013, Los Alamos National Laboratory.
- [21] Knight, E.E., Rougier, E., Munjiza, A., 2013. LANL-CSM: Consortium Proposal for the Advancement of HOSS. Technical Report. LA-UR-13-23409, Los Alamos National Laboratory, 05–09.
- [22] Lakshminarayanan, B., Pritzel, A., Blundell, C., 2017. Simple and scalable predictive uncertainty estimation using deep ensembles, in: Guyon, I., Luxburg, U.V., Bengio, S., Wallach, H., Fergus, R., Vishwanathan, S., Garnett, R. (Eds.), *Advances in Neural Information Processing Systems*, Curran Associates, Inc., pp. 6402–6413. URL: <https://proceedings.neurips.cc/paper/2017/file/9ef2ed4b7fd2c810847ffa5fa85bce38-Paper.pdf>.
- [23] Larkin, K., Rougier, E., Chau, V., Srinivasan, G., Abdelkefi, A., Hunter, A., 2020. Scale bridging damage model for quasi-brittle metals informed with crack evolution statistics. *Journal of the Mechanics and Physics of Solids* 138, 103921. doi:[10.1016/j.jmps.2020.103921](https://doi.org/10.1016/j.jmps.2020.103921).
- [24] Meyer, S., Diegele, E., Brückner-Foit, A., Möslang, A., 2000. Crack interaction modelling. *Fatigue & Fracture of Engineering Materials & Structures* 23, 315–323. doi:[10.1046/j.1460-2695.2000.00283.x](https://doi.org/10.1046/j.1460-2695.2000.00283.x).
- [25] Moore, B.A., Rougier, E., O'Malley, D., Srinivasan, G., Hunter, A., Viswanathan, H., 2018. Predictive modeling of dynamic fracture growth in brittle materials with machine learning. *Computational Materials Science* 148, 46–53. doi:[10.1016/j.commatsci.2018.01.056](https://doi.org/10.1016/j.commatsci.2018.01.056).
- [26] Munjiza, A., 1992. Discrete elements in transient dynamics of fractured media. Ph.D. thesis. Swansea University.
- [27] Munjiza, A., Knight, E.E., Rougier, E., 2015. Large strain finite element method: a practical course. John Wiley & Sons.
- [28] Munjiza, A., Owen, D.R.J., Bicanic, N., 1995. A combined finite-discrete element method in transient dynamics of fracturing solids. *Engineering computations* 12, 145–174. doi:[10.1108/02644409510799532](https://doi.org/10.1108/02644409510799532).
- [29] Munjiza, A.A., 2004. The combined finite-discrete element method. John Wiley & Sons.
- [30] Munjiza, A.A., Knight, E.E., Rougier, E., 2011. *Computational mechanics of discontinua*. John Wiley & Sons.
- [31] Paliwal, B., Ramesh, K., 2008. An interacting micro-crack damage model for failure of brittle materials under compression. *Journal of the Mechanics and Physics of Solids* 56, 896–923. doi:[10.1016/j.jmps.2007.06.012](https://doi.org/10.1016/j.jmps.2007.06.012).
- [32] Panda, N., Osthus, D., Srinivasan, G., O'Malley, D., Chau, V., Oyen, D., Godinez, H., 2020. Mesoscale informed parameter estimation through machine learning: A case-study in fracture modeling. *Journal of Computational Physics* 420, 109719. doi:[10.1016/j.jcp.2020.109719](https://doi.org/10.1016/j.jcp.2020.109719).
- [33] Pedregosa, F., Varoquaux, G., Gramfort, A., Michel, V., Thirion, B., Grisel, O., Blondel, M., Prettenhofer, P., Weiss, R., Dubourg, V., Vanderplas, J., Passos, A., Cournapeau, D., Brucher, M., Perrot, M., Duchesnay, E., 2011. Scikit-learn: Machine learning in Python. *Journal of Machine Learning Research* 12, 2825–2830. URL: <https://www.jmlr.org/papers/volume12/pedregosa11a/pedregosa11a.pdf>.
- [34] Raissi, M., Perdikaris, P., Karniadakis, G.E., 2017. Physics informed deep learning (part I): Data-driven solutions of nonlinear partial differential equations. *arXiv:1711.10561v1[cs.AI]*.
- [35] Rougier, E., Knight, E., Munjiza, A., 2013. LANL-CSM: HOSS-MUNROU Technology Overview. Technical Report. LA-UR-13-23422, Los Alamos National Laboratory, 05–10.
- [36] Rougier, E., Knight, E.E., Broome, S.T., Sussman, A.J., Munjiza, A., 2014. Validation of a three-dimensional finite-discrete element method using experimental results of the split hopkinson pressure bar test. *International journal of rock mechanics and mining sciences* 70, 101–108. doi:[10.1016/j.ijrmms.2014.03.011](https://doi.org/10.1016/j.ijrmms.2014.03.011).
- [37] Rougier, E., Munjiza, A., John, N.W.M., 2004. Numerical comparison of some explicit time integration schemes used in dem, fem/dem and molecular dynamics. *International journal for numerical methods in engineering* 61, 856–879. doi:[10.1002/nme.1092](https://doi.org/10.1002/nme.1092).
- [38] Rougier, E., Munjiza, A., Lei, Z., Chau, V.T., Knight, E.E., Hunter, A., Srinivasan, G., 2020. The combined plastic and discrete fracture deformation framework for finite-discrete element methods. *International Journal for Numerical Methods in Engineering* 121, 1020–1035. doi:[10.1002/nme.6255](https://doi.org/10.1002/nme.6255).
- [39] Schmidt, J., Marques, M.R.G., Botti, S., Marques, M.A.L., 2019. Recent advances and applications of machine learning in solid-state materials science. *npj Computational Materials* 5, 1–36. doi:[10.1038/s41524-019-0221-0](https://doi.org/10.1038/s41524-019-0221-0).
- [40] Smith, R.C., 2013. *Uncertainty Quantification: Theory, Implementation, and Applications*. volume 12. SIAM.
- [41] Srinivasan, G., Hyman, J.D., Osthus, D.A., Moore, B.A., O'Malley, D., Karra, S., Rougier, E., Hagberg, A.A., Hunter, A., Viswanathan, H.S., 2018. Quantifying topological uncertainty in fractured systems using graph theory and machine learning. *Scientific reports* 8, 11665.
- [42] Suthaharan, S., 2014. Big data classification: Problems and challenges in network intrusion prediction with machine learning. *ACM SIGMETRICS Performance Evaluation Review* 41, 70–73. doi:[10.1145/2627534.2627557](https://doi.org/10.1145/2627534.2627557).
- [43] Vaughn, N., Kononov, A., Moore, B., Rougier, E., Viswanathan, H., Hunter, A., 2019. Statistically informed upscaling of damage evolution in brittle materials. *Theoretical and Applied Fracture Mechanics* 102, 210–221. doi:[10.1016/j.tafmec.2019.04.012](https://doi.org/10.1016/j.tafmec.2019.04.012).
- [44] Wang, Y., Cheung, S.W., Chung, E.T., Efendiev, Y., Wang, M., 2020. Deep multiscale model learning. *Journal of Computational Physics* 406, 109071. doi:[10.1016/j.jcp.2019.109071](https://doi.org/10.1016/j.jcp.2019.109071).
- [45] Wilcox, R., 2016. *Introduction to Robust Estimation and Hypothesis Testing*. 4th ed., Academic Press.
- [46] Zhang, D., Lu, L., Guo, L., Karniadakis, G.E., 2019. Quantifying total uncertainty in physics-informed neural networks for solving forward and inverse stochastic problems. *Journal of Computational Physics* 397, 108850. doi:[10.1016/j.jcp.2019.07.048](https://doi.org/10.1016/j.jcp.2019.07.048).
- [47] Zhu, Y., Zabarav, N., 2018. Bayesian deep convolutional encoder-decoder networks for surrogate modeling and uncertainty quantification. *Journal of Computational Physics* 366, 415–447. doi:[10.1016/j.jcp.2018.05.048](https://doi.org/10.1016/j.jcp.2018.05.048).

A. Determination of Contours for Multivariate Normal Distribution

Contours of the multivariate normal distribution are the set of values where the argument of the exponential in the PDF is the same. Therefore, contours correspond to

$$(\mathbf{x} - \boldsymbol{\mu})^T \boldsymbol{\Sigma}^{-1} (\mathbf{x} - \boldsymbol{\mu}) = \gamma,$$

where $\gamma > 0$ is a constant value. For data in \mathbb{R}^2 , each contour corresponds to an ellipse. For simplicity it is assumed that $\boldsymbol{\mu} = \mathbf{0}$ and that the covariance matrix has been diagonalized. Therefore,

$$(\mathbf{x} - \boldsymbol{\mu})^T \boldsymbol{\Sigma}^{-1} (\mathbf{x} - \boldsymbol{\mu}) = \left(\frac{x}{\sigma_x} \right)^2 + \left(\frac{y}{\sigma_y} \right)^2.$$

Integrating the PDF of the multivariate inside the ellipse and requesting it to be equal to a specific coverage yields to

$$\begin{aligned} 4 \int_0^{\sigma_x} \int_0^{\sigma_y \sqrt{\gamma - \left(\frac{x}{\sigma_x}\right)^2}} \frac{1}{2\pi} \frac{1}{\sigma_x \sigma_y} \times \\ \exp \left[-\frac{1}{2} \left(\left(\frac{x}{\sigma_x} \right)^2 + \left(\frac{y}{\sigma_y} \right)^2 \right) \right] dy dx \\ = 1 - \alpha, \end{aligned}$$

where the integral is computed over the quarter ellipse in the first quadrant.

Making the change of variables to

$$\begin{aligned} x &= \sigma_x z \cos \theta \\ y &= \sigma_y z \sin \theta \end{aligned},$$

and computing the Jacobian of the transformation

$$J(z, \theta) = \begin{pmatrix} \frac{\partial x}{\partial z} & \frac{\partial x}{\partial \theta} \\ \frac{\partial y}{\partial z} & \frac{\partial y}{\partial \theta} \end{pmatrix} = \begin{pmatrix} \sigma_x \cos \theta & -\sigma_x z \sin \theta \\ \sigma_y \sin \theta & \sigma_y z \cos \theta \end{pmatrix},$$

and its determinant

$$\det J(z, \theta) = \sigma_x \sigma_y z \cos^2 \theta + \sigma_x \sigma_y z \sin^2 \theta = \sigma_x \sigma_y z,$$

allows for the following substitutions

$$\left(\frac{x}{\sigma_x} \right)^2 + \left(\frac{y}{\sigma_y} \right)^2 = \left(\frac{\sigma_x z \cos \theta}{\sigma_x} \right)^2 + \left(\frac{\sigma_y z \sin \theta}{\sigma_y} \right)^2 = z^2,$$

$$dx dy = \det J(z, \theta) dz d\theta = \sigma_x \sigma_y z dz d\theta.$$

This, in turn, leads to

$$1 - \alpha = \frac{1}{2\pi} \int_0^{\sqrt{\gamma}} z dz e^{-\frac{z^2}{2}} \int_0^{2\pi} d\theta = \int_0^{\sqrt{\gamma}} z e^{-\frac{z^2}{2}} dz.$$

Substituting: $s = -z^2/2$, correspondingly $ds = -z dz$, yields

$$\int_0^{\sqrt{\gamma}} z e^{-\frac{z^2}{2}} dz = \int_{-\frac{\gamma}{2}}^0 e^s ds = \left(1 - e^{-\frac{\gamma}{2}} \right).$$

Then,

$$\begin{aligned} 1 - \alpha &= 1 - e^{-\frac{\gamma}{2}} \\ \Rightarrow \gamma &= -2 \ln \alpha. \end{aligned}$$